EDGE ARTICLE

Check for updates

A supramolecular nanoplatform for imaging-guided phototherapies *via* hypoxia tumour microenvironment remodeling†

Weijie Zhou,‡ Suwen Chen,‡ Yingjie Ouyang, Baoxuan Huang, Hongman Zhang, Weian Zhang* and Jia Tian [ID] *

Photodynamic therapy (PDT) has emerged as an invasive and promising antitumour treatment, however, the hypoxia in deep tumour tissues and the poor water-solubility of photosensitizers as bottlenecks greatly hinder PDT efficiency. Herein, a tumour microenvironment (TME) activated supramolecular nanoplatform consisting of the pillar[5]arene-based amphiphilic polymer POPD, the phototherapeutic agent Cy7-CN, respiratory medication atovaquone (ATO) and chemotherapeutic drug pyridinyl camptothecin (CPT-Py) was constructed for imaging-guided hypoxia-ameliorated phototherapies. Owing to host–guest interaction, the photochemical and photophysical properties of cyanine were improved exceedingly due to the suppression of $\pi-\pi$ stacking. Triggered by the acidic microenvironment in tumour sites, the supramolecular nanoplatform would dissociate and release CPT-Py and ATO which inhibits mitochondria-associated oxidative phosphorylation (OXPHOS) and encourages more oxygen to be used in enhanced PDT. *In vitro* and *in vivo* studies verified that the rational combination of ATO-enhanced PDT and PTT overcame the disadvantages of single phototherapy and formed mutual promotion, and simultaneously sensitized chemotherapeutic drugs, which resulted in high tumour inhibition. It is hoped that the supramolecular nanoplatform could shed light on the development of phototherapeutic agents.

Introduction

As a disease with a high mortality rate, cancers threaten human health continuously, and seriously affect human survival and development.[1–3] To reduce the pain caused by cancer both physically and psychologically, a series of therapeutic methods have been developed, such as surgical treatment, chemotherapy, and radiotherapy.[4–7] Among them, phototherapy, which leads to almost no drug-resistance and no significant side effects to surrounding tissues, has received increasing attention.[8–10] Photodynamic therapy (PDT) relies on that upon light irradiation, photosensitizers transfer the energy or electrons to oxygen molecules to produce singlet oxygen ($^1O_2$), and it emerged as a promising and invasive potential alternative therapy.[11–14] However, hypoxia usually occurs deep in the tumour, where the extremely low oxygen level in the tumour microenvironment (TME) essentially contributes to low PDT efficiency, which results in tumour metastasis and recurrence. To alleviate this situation, various efforts have been made to

relieve tumour hypoxia.[15–19] Most solutions focused on enhancing the oxygen supply, such as physical delivery or *in situ* generation of oxygen, which were hampered by some disadvantages including the limited delivery efficiency of oxygen, the easy inactivation of enzymes involved in oxygen supply *in situ*, and the poor biocompatibility. Recently, respiration has attracted tremendous interest because of its constant consumption of oxygen, leading to the deterioration of the hypoxia TME and the great limitation of PDT effect. Atovaquone (ATO) as a mitochondrial respiratory inhibitor provided a promising way to tackle the hypoxia problem in the TME.[20–23] ATO could inhibit mitochondria-associated oxidative phosphorylation (OXPHOS), the proceeding of which contributed to the expense of oxygen.[24–26] In this way, the hypoxia TME would be improved and more oxygen could be distributed to PDT, leading to better PDT therapeutic effects.

In addition, it is difficult to achieve the desired effect by PDT alone, while combining PDT with other therapeutic modalities such as photothermal therapy and chemotherapy may achieve high efficiency against tumours. Photothermal therapy (PTT), another encouraging therapy, kills cancer cells by heat generated by photothermal reagents upon light irradiation. The local heat generated in PTT can improve the intracellular accumulation of photosensitizers by increasing cell membrane permeability, and alleviate the hypoxic environment of tumours by accelerating blood flow in the irradiation area, thereby

Shanghai Key Laboratory of Functional Materials Chemistry, School of Chemistry and Molecular Engineering, East China University of Science and Technology, 130 Meilong Road, Shanghai 200237, China. E-mail: wazhang@ecust.edu.cn; tianjia@ecust.edu.cn

† Electronic supplementary information (ESI) available. See DOI: https://doi.org/10.1039/d3sc03797e

‡ These authors contributed equally.

improving PDT.[27–29] Meanwhile, as reported, the therapeutic effect of PTT is limited by the heat resistance of tumour cells induced by heat shock proteins (HSPs).[30–32] However, ROS generated in PDT could decrease the heat resistance of HSPs by reducing the production of HSPs.[33–35] Therefore, PDT and PTT can complement each other to mutually enhance the anti-tumour effect. In addition, the ROS produced in PDT and the local heat generated in PTT can promote the cellular uptake of chemotherapeutic drugs, which maximized the activity of chemotherapeutic drugs. Therefore, it is essential to build a multifunctional platform to rationally combine photo-therapeutic treatments.

Supramolecular chemistry, as an efficient tool in the fabrication of functional nanomaterials based on non-covalent interactions, has given rise to great interest in chemistry, biology and materials science due to its reversible and dynamic interactions.[36–40] Among various non-covalent interactions, host–guest interaction has been widely used, which combines host molecules and guest molecules through specific molecular recognition.[41,42] Macrocyclic molecules such as crown ethers, cyclodextrins (CD),[43–45] calixarenes (C[n]A),[46] cucurbitudes (CB[n]),[47–49] and pillararenes (P[n]A) exhibit excellent host–guest capabilities because of their unique resizable cavities. Among these macrocyclic molecules, pillararenes (P[n]A) have attracted wide interest owing to their symmetrical structure and easy modification.[50–58] The electron-rich inner cavity of pillararenes (P[n]A) gave them a high host–guest binding ability, thus providing them with excellent loading potential.[59] Therefore, the construction of a pillararene-based supramolecular nano-platform by host–guest interaction would provide a versatile and promising strategy to intelligently combine multimodal therapies for efficient cancer treatment.

Herein, we proposed and constructed a TME-responsive multifunctional supramolecular platform by host–guest interaction and self-assembly for respiratory regulation enhanced PDT and PTT in hypoxic antitumour treatments (Scheme 1). The P[5]A-containing monomer, TME-responsive monomer, and oligo(ethylene glycol) methyl ether methacrylate were polymerized by RAFT polymerization to fabricate a P[5]-containing TME-responsive amphiphilic polymer (denoted as POPD) which worked as the multipoint host motif. Based on host–guest interaction, the phototherapeutic agent cyano-functionalized cyanine (denoted as Cy7-CN) and the chemotherapeutic drug pyridinyl-functionalized camptothecin (denoted as CPT-Py) were used as the guest motifs to fabricate a supramolecular polymer. The multifunctional platforms (denoted as CyCA@POPD) were obtained by the co-assembly of the supramolecular polymer and mitochondrial respiratory inhibitor ATO in an aqueous solution. The TME-responsive multifunctional supra-molecular platform with respiratory regulation for synergistic O_2-economic promoted PDT, PTT, and chemotherapy has the following advantages: (1) the steric hindrance of the P[5] and Cy7-CN host–guest complex suppressed the aggregation of Cy7, which significantly amplified the photochemical and photophysical properties of Cy7 including the fluorescence, ROS generation and photothermal effect. (2) The encapsulated ATO played the role of a cellular O_2 economizer by breathing
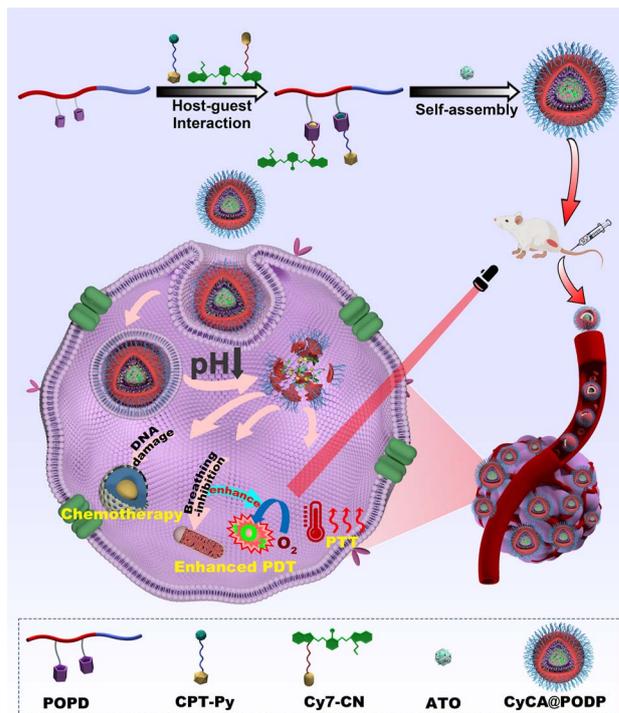
Scheme 1 Schematic illustration of the synthesis of the multifunctional nanoplatform CyCA@POPD consisting of cyanine, CPT, ATO, and P[5]-containing polymers (PODP), and the application in combined PDT, PTT, and chemotherapy.

inhibition of tumour cells for boosted ROS generation in PDT, particularly for hypoxia tumours. (3) TME-triggered dissociation of the supramolecular platform led to the controlled release of CPT, which could be sensitized by the generated ROS for deeper tumour-tissue penetration. (4) The supramolecular platform rationally combined the functions of ATO-boosted PDT, PTT and chemotherapy, resulting in the advantage complementary of each single therapy and better therapeutic efficacy. *In vitro* and *in vivo* studies have been performed to assess the tumour inhibition efficacy of the synergistic trimodal combination therapy.

Results and discussion

Preparation and characterization of CyCA@POPD

To obtain the TME-responsive supramolecular nanoplatform CyCA@POPD for synergistic phototherapy and chemotherapy, the POPD block copolymer was first synthesized by reversible addition-fragmentation chain transfer (RAFT) polymerization of the hydrophobic pillar[5]arene-containing monomer (denoted as P[5]-M), with the water-soluble mono-telechelic polymer POEGMA as a macromolecule RAFT agent (Scheme S1†). The introduction of pillar[5]arene-containing block afforded POPD the ability of host–guest recognition, where POPD worked as a multi-point host macromolecule. Cy7, an NIR cyanine dye, and camptothecin (CPT) were selected as the model photo-therapeutic agent and chemotherapeutic drug, which were

functionalized with guest units, and denoted as Cy7-CN and CPT-Py, respectively (Schemes S2 and S3†). The introduction of the pyridinium group in CPT-Py significantly improved the water-solubility of CPT, which resulted in the deeper tumour penetration and better bioavailability of CPT. The host–guest interaction between Cy7-CN, CPT-Py and the P[5]-containing POPD polymer led to the formation of the amphiphilic supramolecular polymer, which could automatically self-assemble into supramolecular nanoparticles in aqueous solution. The ^{1}H NMR spectra of POPD copolymers, Cy7-CN, CPT-Py, and the related intermediate products, and the GPC curve of POPD copolymers are shown in Fig. S1–S11.†

The nanoprecipitation method was used to prepare the CyCA@POPD nanoparticles according to the host–guest interaction and self-assembly of POPD, Cy7-CN, CPT-Py, and ATO, as shown in Fig. 1A. Owing to the host–guest interaction, Cy7-CN and CPT-Py could be grafted onto POPD, while the followed encapsulation of ATO led to the formation of CyCA@POPD nanoparticles. As shown in Fig. 1B, CyCA@POPD presented the characteristic absorption at the wavelength of 280 nm, 360 nm, and 790 nm, which were corresponding to the absorption of ATO, CPT-Py, and Cy7-CN, respectively, indicating the successful grafting and encapsulation. In addition, since Cy7-CN, CPT-Py and ATO were born with specific absorption, which could be utilized to calculate the loading content (LC) and encapsulation efficiency (EE) of Cy7-CN, CPT-Py, and ATO in CyCA@POPD nanoparticles according to the following formulae:

$$\text{LC}(\%) = \frac{(\text{weight of cargo in nanoparticles})}{(\text{weight of cargo-loaded nanoparticles})} \times 100\% \quad (1)$$

$$\text{EE}(\%) = \frac{(\text{weight of cargo in nanoparticles})}{(\text{weight of cargo in feed})} \times 100\% \quad (2)$$

The standard curves of Cy7-CN, CPT-Py, and ATO were determined by UV-vis spectroscopy and are presented in Fig. S12–S14.† Based on the standard curves and the formulae, the LC and EE of Cy7-CN, CPT-Py and ATO in CyCA@POPD nanoparticles are shown in Table S1.†

The transmission electron microscopy (TEM) images of POPD and CyCA@POPD can be seen in Fig. 1C and D, which both presented their regular and uniform spherical morphologies. Dynamic light scattering (DLS) was then used to evaluate the hydrodynamic sizes of assemblies. As shown in Fig. 1E, the hydrodynamic size of POPD was *ca.* 65 nm, while after encapsulating Cy7-CN, CPT-Py and ATO, the CyCA@POPD nanoparticles exhibited a larger hydrodynamic size of *ca.* 145 nm. Notably, CyCA@POPD showed a good stability in PBS at pH 7.4, whose hydrodynamic size could remain at *ca.* 150 nm for 14 days (Fig. 1F). The stability of CyCA@POPD under the mixture of RPMI-1640 Medium and fetal bovine serum was evaluated by DLS analysis in Fig. S15.† No significant changes in the particle size of CyCA@POPD were observed within 14 d, revealing the excellent stability of nanoparticles in a protein-rich environment.

To achieve effective photodynamic therapy, reactive oxygen species (ROS) generation capability was an essential criterion for photosensitizers. Therefore, 1,3-diphenylisobenzofuran (DPBF) was used as the ROS detector, whose absorbance would be reduced due to the oxidation of ROS. As shown in Fig. 1G and S16,† both POPD and CPT@POPD presented no ROS generation. However, with the loading of Cy7-CN, Cy@POPD and CyCA@POPD assemblies presented excellent ROS generation ability under 808 nm laser light irradiation, which indicated that CyCA@POPD nanoparticles possessed excellent ROS generation capability, which was better than that of free Cy7-CN.
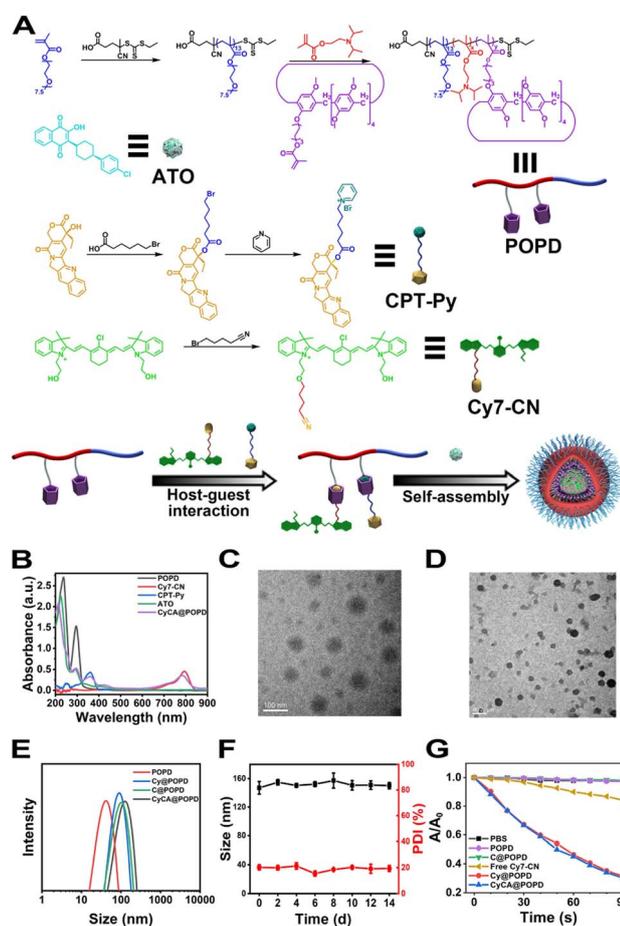

Fig. 1 Synthesis and characterization of CyCA@POPD. (A) Schematic illustration of the synthesis of POPD, Cy7-CN, CPT-Py, and the amphiphilic supramolecular polymer by host–guest interaction, and its self-assembly to form CyCA@POPD supramolecular nanoparticles. (B) UV-vis spectra of POPD, Cy7-CN, CPT-Py, ATO, and CyCA@POPD, respectively. (C) TEM images of POPD, and (D) CyCA@POPD. (E) The hydrodynamic curves of POPD, Cy@POPD, C@POPD, and CyCA@POPD, respectively. (F) The physical stability of CyCA@POPD in PBS (pH = 7.4). Each data point was expressed as mean standard deviation (n = 3). (G) UV-vis spectra of DPBF with PBS, POPD, C@POPD, Cy@POPD and CyCA@POPD under light irradiation (808 nm, 1.0 W cm^{-2}) for predetermined time points.

pH-responsiveness behavior of CyCA@POPD

Considering that the tumour-specific microenvironment (TME) is weakly acidic, the tertiary amine-containing repeat units in POPD could be protonated, which led to the phase transition of

POPD from hydrophobic to hydrophilic (Fig. 2A). Meanwhile, the CyCA@POPD nanoparticles would simultaneously dissociate and release ATO and CPT-Py due to the protonation of POPD and pyridine units in CPT-Py (Fig. 2B). The irregular morphology of CyCA@POPD nanoparticles in pH 5.5 shown in the TEM image confirms the dissociation of CyCA@POPD nanoparticles (Fig. 2C). Moreover, as shown in Fig. 2D, the hydrodynamic size of CyCA@POPD became larger as well as the size polydispersity index (PDI), confirming the pH-triggered dissociation of CyCA@POPD assemblies.

As presented in Fig. 2E, because of the possible precipitation of hydrophobic ATO, the absorption peak of ATO at 290 nm was gradually reduced with the pH decreasing from 7.4 to 5.5. What's more, the absorption of CyCA@POPD at 730 nm increased and the absorption at 790 nm decreased, which indicated that the partial H-aggregates of Cy7 occurred during nanoparticle dissociation and re-assembly induced by the pH reduction. In addition, compared with the neutral environment, the fluorescence of CyCA@POPD assemblies significantly improved in the acidic environment as shown in Fig. 2F, which signified that CyCA@-POPD nanoparticles possessed the capability of fluorescence

bioimaging in a tumour-specific microenvironment. What's more, the zeta potentials of CyCA@POPD assemblies under different pH conditions were measured (Fig. 2G). Owing to the protonation of the pH-responsive tertiary amine units in POPD, CyCA@POPD nanoparticles presented a higher zeta potential at pH 5.5 than that at pH 7.4, which further verified the TME-responsiveness of CyCA@POPD nanoparticles. Then we further analyzed the release profiles of CyCA@POPD under different pH conditions. As shown in Fig. 2H, less than 25% CPT-Py was released under pH 7.4 after 24 h. However, under pH = 5.5, more than 95% CPT-Py was released, demonstrating that CyCA@POPD assemblies could act as a tumour specific microenvironment-targeted drug delivery system with low side effects to normal tissues. Moreover, the ROS generation capability of CyCA@POPD under different pH conditions was also evaluated using DPBF as the ROS detector and the results are shown in Fig. S17.† It could be seen that the dissociation of CyCA@POPD in a weakly acidic environment exhibited an ignorable influence on its ROS generation capability.

Assessment of photothermal effect of CyCA@POPD

It's known that cyanine dyes not only have a good photodynamic effect but also exhibit a promising photothermal effect, which have been recognized as a typical organic photothermal agent. As shown in Fig. 3A, the temperature of the CyCA@POPD sample increased sharply upon 808 nm light irradiation, while only *ca.* 10 °C temperature increase was found from the small molecular compound Cy7 sample. Moreover, the photothermal effects of POPD, C@POPD, Cy7, Cy@POPD and CyCA@POPD samples were tested and the real-time temperatures of all the samples were recorded as shown in Fig. 3B. Obviously, the temperatures of PBS, POPD and C@POPD solution presented insignificant changes, since there were no photothermal agents in them. Notably, the temperatures of Cy@POPD and CyCA@-POPD samples presented a more significant rise upon light irradiation than that of Cy7, which illustrated that the host–guest interaction between Cy7-CN and POPD, and the self-assembly of Cy@POPD and CyCA@POPD samples led to better stability and stronger photothermal effect of Cy7. What's more, the photothermal conversion efficiency (PCE) of CyCA@POPD assemblies was calculated in Fig. 3C, which shows that the temperature of the CyCA@POPD assembly solution rose to 50 °C when the concentration of Cy7-CN was 20 μg mL^{-1} under light irradiation for 5 min (808 nm, 1.0 W cm^{-2}), presenting a high PCE of 37%. In addition, the temperature rise also exhibited a positive correlation with the concentration of CyCA@POPD and the light intensity (Fig. 3D and E). In addition, benefiting from the stable host–guest interaction between Cy7-CN and the amphiphilic polymer POPD, the variation of the pH value had negligible influence on the temperature rise (Fig. 3F). This indicated that Cy7-CN in CyCA@POPD possessed good biostability and high photothermal effect either in blood circulation or within tumour cells. Thus, CyCA@POPD nanoparticles exhibited excellent ROS generation ability and photothermal effect upon 808 nm laser light irradiation, exhibiting great potential in anti-tumour treatment.
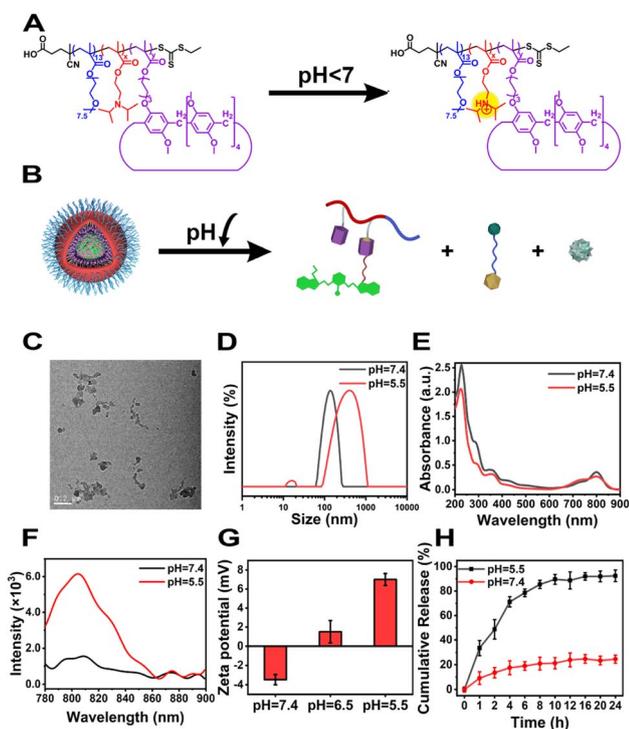

Fig. 2 TME-responsive behavior of CyCA@POPD. (A) Schematic illustration of the protonation mechanism of CyCA@POPD assemblies. (B) Schematic illustration of the responsive behavior of CyCA@POPD assemblies under different pH conditions. (C) TEM image of CyCA@-POPD assemblies at pH = 5.5. (D) Hydrodynamic size of CyCA@POPD assemblies under different pH conditions. (E) UV-vis spectra of CyCA@POPD assemblies under different pH conditions. (F) Fluorescence spectra of CyCA@POPD assemblies under different pH in aqueous solutions at room temperature (Ex: 750 nm). (G) Zeta potentials of CyCA@POPD assemblies in PBS solution under different pH conditions. (H) CPT-Py release profiles from CyCA@POPD assemblies under different pH conditions.
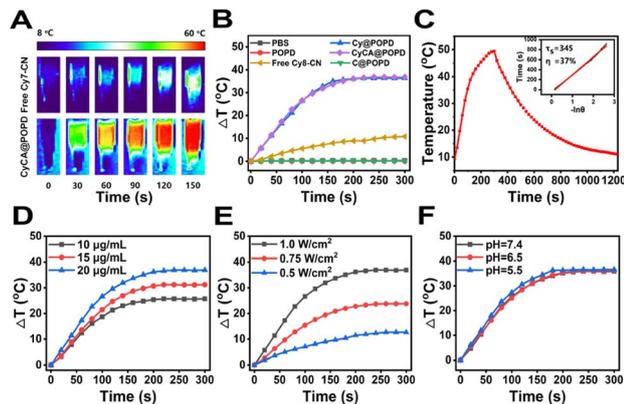
Fig. 3 Photothermal behavior of CyCA@POPD. (A) Infrared thermography of CyCA@POPD assemblies irradiated with an 808 nm laser (1.0 W cm^{-2}). (B) Photothermal effect of different assemblies under light irradiation (808 nm, 1.0 W cm^{-2}). (C) Calculation of the photothermal conversion efficiency (PCE) of CyCA@POPD assemblies. Photo-thermal effect of CyCA@POPD assemblies at different concentrations (D) and upon light irradiation with different power densities (E). (F) Photothermal effect of CyCA@POPD assemblies under different pH conditions upon light irradiation (808 nm, 1.0 W cm^{-2}).

Cellular uptake and intracellular ROS generation of CyCA@POPD

To evaluate the cellular uptake of the CyCA@POPD nanoparticles against 4T1 cells, the images of confocal laser scanning microscopy (CLSM) were analyzed. After incubation with free Cy7-CN molecules, Cy@POPD nanoparticles and CyCA@POPD nanoparticles, the 4T1 cells were fixed in paraformaldehyde (PFA) and the nuclei of 4T1 cells were stained with 4′,6-diamidino-2-phenylindole (DAPI). As shown in Fig. 4A, brighter fluorescence of 4T1 cells was observed after being cultured with Cy@POPD and CyCA@POPD nanoparticles, which indicated that the cellular uptake of Cy@POPD and CyCA@POPD was more than the uptake of Cy7-CN by 4T1 cells. In order to better illustrate the cellular uptake difference between the samples, the mean fluorescence intensity of cells was summarized and is shown in Fig. 4B, in which cells treated with CyCA@POPD exhibited the highest fluorescence intensity and significant difference compared with the other samples. This phenomenon was mainly attributed to that the endocytosis of Cy@POPD and CyCA@POPD was faster and easier than the diffusion of hydrophobic Cy7-CN molecules. Particularly, because of the acidic nature of endosomal vesicles, the POPD polymers in CyCA@POPD nanoparticles exhibited a "proton sponge effect", in which POPD switched from hydrophobic and uncharged to hydrophilic and positively charged, leading to endosomal swelling and lysis, and thus the endosomal escape and higher internalization of CyCA@POPD.

Benefiting from the enhanced internalization of CyCA@POPD, the intracellular ROS generation of CyCA@POPD nanoparticles was further studied. 2′,7′-Dichlorodihydro-fluorescein diacetate (DCFH-DA) was utilized as the ROS probe. As shown in Fig. 4C, almost no fluorescence was observed in the control group with 808 nm laser light irradiation. Strong green fluorescence was presented in the CyC@POPD group, which
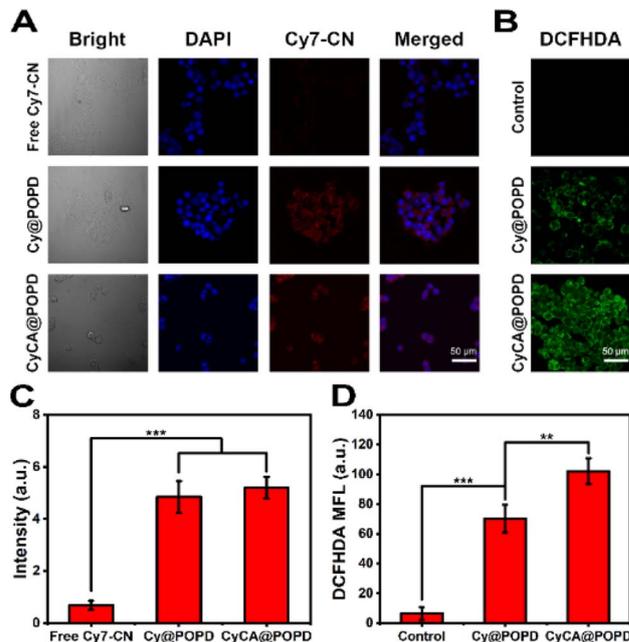

Fig. 4 The cellular uptake and intracellular ROS generation of CyCA@POPD. (A) CLSM images of 4T1 cells incubated with different samples: (a) free Cy7-CN, (b) Cy@POPD assemblies, and (c) CyCA@POPD assemblies for 24 h. (B) CLSM images of intracellular ROS generation in 4T1 cells after being cultured with different samples with light irradiation (808 nm, 0.5 W cm^{-2}, 5 min): (a) control, (b) Cy@POPD nanoparticles and (c) CyCA@POPD nanoparticles. (C) The comparison of mean fluorescence intensities of cellular uptake with different samples based on CLSM images. (D) The comparison of mean fluorescence intensities of CLSM images of intracellular ROS generation. Scale bar: 50 μm.

contributed to the great ROS generation capability of Cy7-CN units of CyC@POPD nanoparticles. What's more, with encapsulating ATO in CyCA@POPD nanoparticles, the brightest green fluorescence was observed in cells treated with CyCA@POPD nanoparticles. This was mainly because of the good internalization of CyCA@POPD and the pH-triggered ATO release, which could block mitochondria-associated oxidative phosphorylation and relieve hypoxia in tumour cells. The comparison of mean fluorescence intensity in the cells treated with different formulae is shown in Fig. 4D, which demonstrated the significant difference between CyC@POPD and CyCA@POPD groups. Obviously, upon the encapsulation of ATO, the ROS generation of the CyCA@POPD group was remarkably higher than that of the CyC@POPD group because of the enhanced PDT induced by the ATO-based oxygen economizer. Thus, CyCA@POPD not only exhibited efficient internalization, but also intracellular ROS generation, indicating the promising therapeutic efficacy of CyCA@POPD.

In vitro cytotoxicity of CyCA@POPD

Encouraged by the excellent intracellular ROS generation capability and competent cellular uptake of CyCA@POPD, the *in vitro* cytotoxicity estimation of CyCA@POPD was explored by the 3-(4,5-dimethylthiazol-2-yl)-2,5-diphenyltetrazolium bromide

(MTT) assay. It can be seen in Fig. 5A that the without light irradiation POPD group and Cy@POPD group showed no obvious cytotoxicity, which indicated that POPD and Cy@POPD had excellent biocompatibility. In comparison, CyA@POPD and CyC@POPD exhibited cytotoxicity to some extent. This phenomenon was caused by the acidic TME that induced the release of CPT-Py and ATO, which were responsible for chemotherapy and breathing inhibition, respectively. Understandably, the CyCA@POPD group presented a little higher 4T1 cytotoxicity than others in the dark due to the simultaneous TME-triggered CPT-Py delivery and ATO-based breathing inhibition. Particularly, CyCA@POPD showed no significant cytotoxicity in the dark to normal cells such as L929 cells, which demonstrated the good biocompatibility of CyCA@POPD (Fig. S18†). Then, upon exposure to light irradiation, remarkable phototoxicity was presented by the cargo-loaded supramolecular nanoparticle groups. As shown in Fig. 5B, 4T1 cells treated with POPD presented almost no photocytotoxicity. The Cy@POPD group had obvious phototoxicity because of the presence of Cy7-CN, which possessed both of photodynamic and photothermal effects. What's more, compared with the Cy@POPD group, there was a lower cell viability from the CyA@POPD group because of the enhanced PDT induced by the released ATO as the O$_2$ economizer. Of course, a similar result was presented in the CyC@POPD group with the combination of PDT, PTT and chemotherapy. There was no doubt that the CyCA@POPD group possessed the highest phototoxicity, in which more than 80% of 4T1 cells were dead, as a consequence of the combination of enhanced PDT, PTT and chemotherapy. Additionally, to better prove the therapeutic efficacy of CyCA@POPD nanoparticles in the treatment of hypoxia tumour sites, we also researched the dark cytotoxicity and phototoxicity of CyCA@POPD nanoparticles in a hypoxia environment against 4T1 cells. As shown in Fig. 5C, the cell viability in the dark was higher compared to that under normoxia. Without

light irradiation, the CyCA@POPD group exhibited a relatively high cell viability under hypoxia conditions. However, the comparison of Cy@POPD, CyC@POPD, CyA@POPD and CyCA@POPD groups under light irradiation clearly presented that the CyCA@POPD group possessed much higher phototoxicity than the other groups as shown in Fig. 5D. As a result, owing to the combination of enhanced PDT, PTT, and chemotherapy, the CyCA@POPD group with light irradiation possessed the lowest cell viability in the hypoxic environment, which was similar to the phenomenon under normoxia conditions. As shown in Fig. 5E, CyCA@POPD nanoparticles could dissociate in an acidic TME and release CPT-Py and ATO. On one hand, the released CPT-Py could induce DNA damage as a DNA topoisomerase I inhibitor of cancer cells (Chemotherapy). On the other hand, ATO could inhibit the expense of oxygen by blocking mitochondria-associated oxidative phosphorylation to overcome the side effect of hypoxia in a tumour environment and promote the PDT of Cy7-CN. As a result, the light irradiation and adequate O$_2$ conducted the O$_2$-sufficient enhanced PDT of CyCA@POPD. Thus, the combination of enhanced PDT and PTT of Cy7, and TME-triggered delivery of CPT led to the high therapeutic efficacy of CyCA@POPD, indicating that these supramolecular nanoparticles are potential candidate multifunctional platforms for combinational therapies.

In vivo antitumour effect and biosafety of CyCA@POPD

Encouraged by the excellent results of *in vitro* studies of CyCA@POPD nanoparticles, we further assessed the *in vivo* antitumour effect of CyCA@POPD supramolecular nanoparticles on 4T1-tumour-bearing nude mice. Before performing *in vivo* experiments, we analysed the hemolysis of CyCA@POPD nanoparticles. As shown in Fig. S19,† the hemolysis rate of the nanoparticles did not exceed 5% at any of the different concentrations, indicating the good biocompatibility of CyCA@POPD. Then, the process of the antitumour experiment is shown in Fig. 6A. The mice were separated into five groups (n = 4) randomly, which consist of PBS, CyCA@POPD (chemotherapy), CyA@POPD with light irradiation (enhanced PDT + PTT), CyC@POPD with light irradiation (PDT + PTT + chemotherapy), and CyCA@POPD with light irradiation (enhanced PDT + PTT + chemotherapy). First of all, the accumulation of CyCA@POPD at tumour sites was studied by fluorescence imaging *in vivo*, which was conducted at different time points after the different formula being injected through the tail vein. As shown in Fig. 6B, the increased fluorescence intensity in the tumour site could be observed with the extension of time. The fluorescence intensity in the tumour tissues was collected and is represented in the form of a bar graph in Fig. 6C. The fluorescence intensity reached a maximum at 24 h, which revealed that the CyCA@POPD nanoparticles could be accumulated at the tumour site due to the enhanced permeability and retention (EPR) effect. Therefore, it was a suitable method to conduct light irradiation for phototherapies after the nanoparticles were injected for 24 h. In order to compare the tumour inhibition of different formulae, the mice of each group were sacrificed on
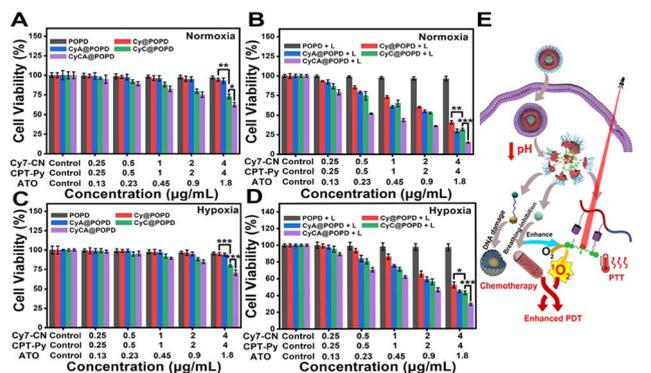

Fig. 5 *In vitro* cytotoxicity of CyCA@POPD by synergistic therapy. (A) The cell viability of 4T1 cells treated with various samples in the dark and (B) upon 808 nm laser light irradiation (500 mW cm^{-2}, 10 min) under normoxia conditions. (C) The cell viability of 4T1 cells treated with various samples in the dark and (D) upon 808 nm laser light irradiation (500 mW cm^{-2}, 10 min) under hypoxia conditions. (E) Schematic illustration of the combination of O$_2$-economizer enhanced PDT, PTT, and chemotherapy of CyCA@POPD.
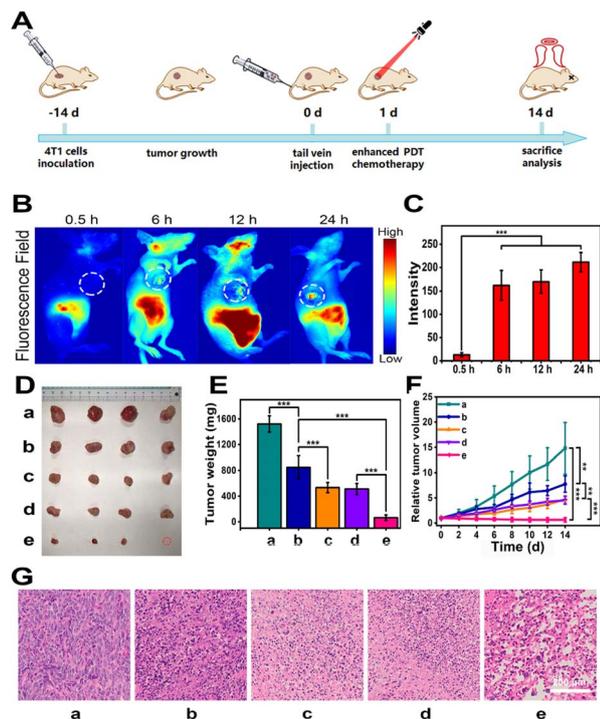
Fig. 6 *In vivo* bioimaging and antitumour therapy. (A) *In vivo* antitumour effect against 4T1-tumour-bearing nude mice. The mice were separated into five groups randomly (*n* = 4): group a, PBS; group b, CyCA@POPD without light (chemotherapy); group c, CyA@POPD with light irradiation (enhanced PDT and PTT); group d, CyC@POPD with light irradiation (PDT, PTT and chemotherapy); group e, CyCA@POPD with light irradiation (enhanced PDT, PTT and chemotherapy). (A) Schematic illustration of the timeline for the antitumour treatment process. (B) Fluorescence images of mice after being injected with CyCA@POPD nanoparticles at 0.5 h, 6 h, 12 h, and 24 h. (C) Mean fluorescence intensity in tumour sites at different time points. (D) Physical photo of tumour tissues on the 14th day after various treatments. (E) Tumour weight of the nude mice after being treated with various samples on the 14th day. (F) Tumour growth lines of mice after being treated with different samples. (G) H&E staining images of tumour tissues after different treatments. Scale bar: 200 μm.

the 14th day after treatments and the tumour tissues were dissected and analysed. The photograph and the tumour weight of anatomical tumour tissues are shown in Fig. 6D and E, respectively. Obviously, compared with the groups of PBS and CyCA@POPD without light irradiation, the other groups including CyA@POPD with light irradiation, CyC@POPD with light irradiation, and CyCA@POPD with light irradiation showed a significant tumour inhibition effect. Particularly, the group of CyCA@POPD with light irradiation exhibited the highest tumour therapeutic efficacy, owing to the effective triple-combination of enhanced PDT, PTT, and chemotherapy. Moreover, the tumour growth volume was recorded every other day and is shown in Fig. 6F, which confirmed the effective antitumour effect of CyCA@POPD with light irradiation throughout the treatment and prognosis stages.

The hematoxylin and eosin (H&E) staining images of tumour tissues are presented in Fig. 6G, in which serious damage in the tumour tissues was demonstrated obviously in the group of

CyCA@POPD nanoparticles with light irradiation. Additionally, the body weights of all mice were recorded every two days and are shown in Fig. S20.† There were negligible changes in the average body weight of mice, which verified the good life security and biosafety of the combinational therapies. Meanwhile, H&E staining images of the major organs in each group are presented in Fig. S21,† including the heart, lung, spleen, kidney and liver. And no obvious physiological structural damage was observed. All results signified that CyCA@POPD nano-particles exhibited low biotoxicity to normal tissues which was essential for further clinical application. Thus, the CyCA@POPD supramolecular nanoparticle with the triple-combination of boosted PDT, PTT, and chemotherapy not only possessed a high antitumour effect, but also good biosafety, which provides a promising pathway for tumour treatments.

Conclusions

In summary, a TME-responsive supramolecular nano-platform CyCA@POPD was constructed by host–guest interaction between Cy7-CN, CPT-Py, ATO and POPD for the combination of respiratory-inhibition enhanced PDT, PTT, and chemotherapy. The supramolecular nanoplatform could dissociate in the tumour-specific microenvironment with low pH and release photo-sensitizers and drugs, leading to precise treatment and negligible side effects. On one hand, the breathing inhibition caused by released ATO could reduce the tumour energy supply and suppress tumour growth. On the other hand, more oxygen was applied for enhanced PDT and promoted antitumour efficacy. What's more, the PTT effect of CyCA@POPD promoted the therapeutic efficiency of PDT and chemotherapy. Significant combinational therapy efficacy and good biosafety of the CyCA@POPD nanoplatform were observed from *in vitro* and *in vivo* studies. Thus, this work provided a novel strategy for developing high-performance combination therapies, which would show promising potential in clinical antitumour treatments.

Data availability

The ESI† contains detailed description for experimental techniques used. Supplementary spectra (including ^{1}H NMR, GPC, UV-vis, and DLS), hemolysis, body weight variation and H&E staining images of major organs are also provided.

Author contributions

Weijie Zhou and Suwen Chen performed the manuscript writing, characterization experiments, data processing and analysis. Yingjie Ouyang performed some of the chemical synthesis, and characterization experiments. Hongman Zhang performed some of chemical synthesis. Baoxuan Huang checked and validated the data. The work was supervised by Jia Tian, and conceived by Weian Zhang and Jia Tian. The manuscript was revised by Baoxuan Huang, Weian Zhang, and Jia

Tian. All authors analyzed the data and commented on the manuscript.

Conflicts of interest

There are no conflicts to declare.

Acknowledgements

Notes and references

1 H. H. Han, H. M. Wang, P. Jangili, M. Li, L. Wu, Y. Zang, A. C. Sedgwick, J. Li, X. P. He, T. D. James and J. S. Kim, *Chem. Soc. Rev.*, 2023, **52**, 879–920.

2 R. Vankayala and K. C. Hwang, *Adv. Mater.*, 2018, **30**, 1706320.

3 H. Yang, R. Liu, Y. Xu, L. Qian and Z. Dai, *Nano-Micro Lett.*, 2021, **13**, 35.

4 A. R. Pradipta, P. Ahmadi, K. Terashima, K. Muguruma, M. Fujii, T. Ichino, S. Maeda and K. Tanaka, *Chem. Sci.*, 2021, **12**, 5438–5449.

5 N. Wang, Z. Deng, Q. Zhu, J. Zhao, K. Xie, P. Shi, Z. Wang, X. Chen, F. Wang, J. Shi and G. Zhu, *Chem. Sci.*, 2021, **12**, 14353–14362.

6 B. Liu, X. Zhang, J. Li, S. Yao, Y. Lu, B. Cao and Z. Liu, *ACS Appl. Mater. Interfaces*, 2022, **14**, 7636–7645.

7 H. Hou, D. Tang, L. Zhang, D. Zhao, H. Xiao and B. Li, *Nano Today*, 2023, **50**, 101858.

8 H. Shi and P. J. Sadler, *Br. J. Cancer*, 2020, **123**, 871–873.

9 X. Zhen, P. Cheng and K. Pu, *Small*, 2019, **15**, 1804105.

10 Q. Zheng, X. Liu, Y. Zheng, K. W. K. Yeung, Z. Cui, Y. Liang, Z. Li, S. Zhu, X. Wang and S. Wu, *Chem. Soc. Rev.*, 2021, **50**, 5086–5125.

11 W. Y. Li, J. J. Wan, J. L. Kan, B. Wang, T. Song, Q. Guan, L. L. Zhou, Y. A. Li and Y. B. Dong, *Chem. Sci.*, 2023, **14**, 1453–1460.

12 Z. Ma, R. An, M. Chen, X. Wang and M. Zhu, *Biomacromolecules*, 2022, **23**, 5074–5083.

13 Q. Ren, Z. Liang, X. Jiang, P. Gong, L. Zhou, Z. Sun, J. Xiang, Z. Xu, X. Peng, S. Li, W. Li, L. Cai and J. Tang, *Int. J. Biol. Macromol.*, 2019, **130**, 845–852.

14 J. Wang, H. Wu, Q. Zhao, Y. Zou, D. Ding, H. Yin and H. Xu, *ACS Appl. Mater. Interfaces*, 2022, **14**, 29613–29625.

15 C. Lai, B. Luo, J. Shen and J. Shao, *Pharmacol. Res.*, 2022, **186**, 106551.

16 Y. Wan, L. H. Fu, C. Li, J. Lin and P. Huang, *Adv. Mater.*, 2021, **33**, 2103978.

17 M. Yi, B. Xiong, Y. Li, W. Guo, Y. Huang and B. Lu, *Eur. J. Med. Chem.*, 2023, **247**, 115084.

18 L. Hong, J. Li, Y. Luo, T. Guo, C. Zhang, S. Ou, Y. Long and Z. Hu, *Biomolecules*, 2022, **12**, 81.

19 L. Larue, B. Myrzakhmetov, A. Ben-Mihoub, A. Moussaron, N. Thomas, P. Arnoux, F. Baros, R. Vanderesse, S. Acherar and C. Frochot, *Pharmaceuticals*, 2019, **12**, 163.

20 W. Feng, S. Zhang, Y. Wan, Z. Chen, Y. Qu, J. Li, T. D. James, Z. Pei and Y. Pei, *ACS Appl. Mater. Interfaces*, 2022, **14**, 20749–20761.

21 W. Gao, J. Zhang, W. Wang, Z. Liu, M. Chen, X. Hu, L. Zeng, C. Zheng, H. Song and Q. Zhang, *Int. J. Pharm.*, 2022, **621**, 121775.

22 C. Ren, X. Xu, D. Yan, M. Gu, J. Zhang, H. Zhang, C. Han and L. Kong, *Acta Biomater.*, 2022, **146**, 465–477.

23 P. Yuan, F. A. Deng, Y. B. Liu, R. R. Zheng, X. N. Rao, X. Z. Qiu, D. W. Zhang, X. Y. Yu, H. Cheng and S. Y. Li, *Adv. Healthcare Mater.*, 2021, **10**, 2100198.

24 Y. T. Fan, T. J. Zhou, P. F. Cui, Y. J. He, X. Chang, L. Xing and H. L. Jiang, *Adv. Funct. Mater.*, 2019, **29**, 1806708.

25 D. Xia, P. Xu, X. Luo, J. Zhu, H. Gu, D. Huo and Y. Hu, *Adv. Funct. Mater.*, 2019, **29**, 1807294.

26 L. P. Zhao, R. R. Zheng, H. Q. Chen, L. S. Liu, X. Y. Zhao, H. H. Liu, X. Z. Qiu, X. Y. Yu, H. Cheng and S. Y. Li, *Nano Lett.*, 2020, **20**, 2062–2071.

27 Y. Ding, C. Du, J. Qian and C. M. Dong, *Nano Lett.*, 2019, **19**, 4362–4370.

28 C. Huang, Z. Zhang, Q. Guo, L. Zhang, F. Fan, Y. Qin, H. Wang, S. Zhou, W. Ou-Yang, H. Sun, X. Leng, X. Pan, D. Kong, L. Zhang and D. Zhu, *Adv. Healthcare Mater.*, 2019, **8**, 1900840.

29 W. Tao, N. Wang, J. Ruan, X. Cheng, L. Fan, P. Zhang, C. Lu, Y. Hu, C. Che, D. Sun, J. Duan and M. Zhao, *ACS Appl. Mater. Interfaces*, 2022, **14**, 6404–6416.

30 Y. Xia, Y. Wu, J. Cao, J. Wang, Z. Chen, C. Li and X. Zhang, *ACS Biomater. Sci. Eng.*, 2022, **8**, 1892–1906.

31 Z. Yu, X. Meng, S. Zhang, X. Wang, Y. Chen, P. Min, Z. Zhang and Y. Zhang, *Biomater. Sci.*, 2021, **10**, 158–166.

32 G. Zhang, W. Cheng, L. Du, C. Xu and J. Li, *J. Nanobiotechnol.*, 2021, **19**, 9.

33 G. Yang, M. Li, T. Song, X. Chen, H. Zhang, X. Wei, N. Li, T. Li, X. Qin, S. Li, F. You, C. Wu, W. Zhang, Y. Liu and H. Yang, *Adv. Healthcare Mater.*, 2022, **11**, 2201615.

34 Y. Zou, D. Huang, S. He, X. Song, W. Liu, W. Sun, J. Du, J. Fan and X. Peng, *Chem. Sci.*, 2023, **14**, 1010–1017.

35 J. Su, T. Liao, Z. Ren, Y. Kuang, W. Yu, Q. Qiao, B. Jiang, X. Chen, Z. Xu and C. Li, *Int. J. Biol. Macromol.*, 2023, **238**, 124088.

36 H. Zhang, J. Zhu, T. Fang, M. Li, G. Chen and Q. Chen, *J. Mater. Chem. B*, 2022, **10**, 7183–7193.

37 J. Zhou, L. Rao, G. Yu, T. R. Cook, X. Chen and F. Huang, *Chem. Soc. Rev.*, 2021, **50**, 2839–2891.

38 H. Jin, X. Lin, M. Gao, L. Cui and Y. Liu, *Front. Chem.*, 2020, **8**, 824.

39 J. Tian, B. Huang, M. H. Nawaz and W. Zhang, *Coordin. Chem. Rev.*, 2020, **420**, 213410.

40 X. Li, S. Lee and J. Yoon, *Chem. Soc. Rev.*, 2018, **47**, 1174–1188.

41 Y. Deng, F. Jia, X. Chen, Q. Jin and J. Ji, *Small*, 2020, **16**, 2001747.

42 D. Hu, Y. Deng, F. Jia, Q. Jin and J. Ji, *ACS Nano*, 2020, **14**, 347–359.

43 A. Ben Mihoub, L. Larue, A. Moussaron, Z. Youssef, L. Colombeau, F. Baros, C. Frochot, R. Vanderesse and S. Acherar, *Molecules*, 2018, **23**, 1936.

44 A. Ikeda, S. Satake, T. Mae, M. Ueda, K. Sugikawa, H. Shigeto, H. Funabashi and A. Kuroda, *ACS Med. Chem. Lett.*, 2017, **8**, 555–559.

45 X. Wu, Y. Chen, Q. Guo, L. Tao, Y. Ding, X. Ding and X. Shen, *Pharmaceutics*, 2022, **14**, 1375.

46 H. T. Feng, Y. Li, X. Duan, X. Wang, C. Qi, J. W. Y. Lam, D. Ding and B. Z. Tang, *J. Am. Chem. Soc.*, 2020, **142**, 15966–15974.

47 O. A. A. Alabrahim, S. A. Fahmy and H. M. E.-S. Azzazy, *Acs. Appl. Nano. Mater.*, 2023, **6**, 3139–3158.

48 X. Wu, M. Liu, J. Niu, Q. Liu, X. Jiang, Y. Zheng, Y. Qian, Y. M. Zhang, J. Shen and Y. Liu, *Chem. Sci.*, 2023, **14**, 1724–1731.

49 H. Yang, Z. Duan, F. Liu, Z. Zhao and S. Liu, *ACS Macro Lett.*, 2023, **12**, 295–301.

50 W. Feng, M. Jin, K. Yang, Y. Pei and Z. Pei, *Chem. Commun.*, 2018, **54**, 13626–13640.

51 F. Lu, Y. Chen, B. Fu, S. Chen and L. Wang, *Chin. Chem. Lett.*, 2022, **33**, 5111–5115.

52 L. Shao, Y. Pan, B. Hua, S. Xu, G. Yu, M. Wang, B. Liu and F. Huang, *Angew Chem. Int. Ed. Engl.*, 2020, **59**, 11779–11783.

53 C. Wang, H. Li, J. Dong, Y. Chen, X. Luan, X. Li and X. Du, *Chemistry*, 2022, **28**, 202202050.

54 K. Wang, X. Tian, J. H. Jordan, K. Velmurugan, L. Wang and X.-Y. Hu, *Chin. Chem. Lett.*, 2022, **33**, 89–96.

55 Q. Yang, W. Xu, M. Cheng, S. Zhang, E. G. Kovaleva, F. Liang, D. Tian, J. A. Liu, R. M. Abdelhameed, J. Cheng and H. Li, *Chem. Commun.*, 2022, **58**, 3255–3269.

56 B. Lu, Z. Zhang, Y. Huang, Y. Zhang, J. Wang, Y. Ding, Y. Wang and Y. Yao, *Chem. Commun.*, 2022, **58**, 10353–10356.

57 J. Tian, L. Xia, J. Wu, B. Huang, H. Cao and W. Zhang, *ACS Appl. Mater. Interfaces*, 2020, **12**, 32352–32359.

58 L. Xia, J. Tian, T. Yue, H. Cao, J. Chu, H. Cai and W. Zhang, *Adv. Healthcare Mater.*, 2022, **11**, 2102015.

59 Y. Yin, P. Sun, H. Dong, Y. Chen, S. Chen and L. Wang, *Chin. Chem. Lett.*, 2023, **34**, 108594.